

FuseDiff: Symmetry-Preserving Joint Diffusion for Dual-Target Structure-Based Drug Design

Jianliang Wu
Sun Yat-sen University
Guangzhou, China

Anjie Qiao
Sun Yat-sen University
Guangzhou, China

Zhen Wang
Sun Yat-sen University
Guangzhou, China

Zhewei Wei
Renmin University of China
Beijing, China

Sheng Chen
Tsinghua University
Beijing, China

Abstract

Dual-target structure-based drug design aims to generate a single ligand together with two pocket-specific binding poses, each compatible with a corresponding target pocket, enabling polypharmacological therapies with improved efficacy and reduced resistance. Existing approaches typically rely on staged pipelines, which either decouple the two poses via conditional-independence assumptions or enforce overly rigid correlations, and therefore fail to jointly generate two target-specific binding modes. To address this, we propose FUSEDIFF, an end-to-end diffusion model that jointly generates a ligand molecular graph and two pocket-specific binding poses conditioned on both pockets. FUSEDIFF features a message-passing backbone with Dual-target Local Context Fusion (DLCF), which fuses each ligand atom’s local context from both pockets to enable expressive joint modeling while preserving the desired symmetries. Together with explicit bond generation, FUSEDIFF enforces topological consistency across the two poses under a shared graph while allowing target-specific geometric adaptation in each pocket. To support principled training and evaluation, we derive a dual-target training set and use an independent held-out test set for evaluation. Experiments on the benchmark and a real-world dual-target system show that FUSEDIFF achieves state-of-the-art docking performance and enables the first systematic assessment of dual-target pose quality prior to docking-based pose search.

1 Introduction

Structure-based drug design (SBDD) exploits the three-dimensional structure of a biological target to design ligands with high affinity and selectivity for a given binding site [2]. While traditional SBDD has largely centered on a single target, the growing demand for polypharmacological agents that improve therapeutic efficacy and delay drug resistance [18, 40] has increasingly motivated dual-target drug design. Accordingly, **dual-target SBDD** seeks to design a single ligand together with *two target-specific binding poses*, each compatible with its corresponding pocket.

With this goal, dual-target SBDD can be cast as conditional density estimation—one of the most natural and general formulations—namely learning $p(G, X_1, X_2 | P_1, P_2)$, where P_1, P_2 denote the two target pockets, G denotes the ligand molecular graph, and X_1, X_2 denote the corresponding binding poses. In contrast to search-based approaches that explore chemical space via multi-objective scoring [6, 35], this formulation directly supports de novo design and produces target-specific binding modes end-to-end, rather than treating pose recovery as a downstream docking step. Another

common shortcut is to reuse single-target generative models sequentially (or to combine their signals); when the first-stage sampling cannot account for the second pocket, the overall procedure can degrade into a nested-loop search over candidates, incurring substantial computational overhead.

Therefore, dedicated dual-target methods are needed. Existing methods often adopt a two-stage pipeline: they first generate 2D molecular graphs (or SMILES) conditioned on both targets using chemical language models or synthesis-aware search, and then recover 3D binding poses via post-hoc optimization or separate single-target pose predictors [36]. This design amounts to modeling $p(G | P_1, P_2)$ and then inferring X_1 and X_2 separately given (G, P_1) and (G, P_2) , which largely decouples pose generation across targets and leaves little room to model cross-target coupling at the pose level. In practice, the noise in paired pose observations (i.e., their experimental structures) tends to be correlated, making this conditional independence assumption restrictive. Moreover, the staged procedure is prone to error accumulation.

To jointly generate ligand atom types and binding poses, Zhou et al. [41] reprogram a pretrained single-target diffusion model by composing predicted scores conditioned on each pocket. To make this strategy viable, it requires explicit geometric alignment of the two pockets via a rigid transformation \mathcal{T} estimated by probe-ligand docking. The resulting sampling effectively targets a composed conditional $p(G, X | P_1, \mathcal{T}P_2)$, implicitly assuming the two target-specific poses are compatible under a single rigid transformation, which mismatches real dual-target pose distributions. Consequently, the raw sampled poses can deviate substantially from the true binding modes and require docking-based conformational search to recover two poses, partially degenerating back to a two-stage pipeline.

In this work, we aim to learn $p(G, X_1, X_2 | P_1, P_2)$ in a genuinely end-to-end manner, while avoiding the restriction/assumption above to improve expressiveness. To this end, we identify two fundamental obstacles. First, dual-target SBDD datasets that explicitly support learning this density are scarce, as such data must jointly specify the ligand identity and paired binding poses across targets. Second, jointly generating target-specific poses together with their shared molecular graph requires the model to introduce appropriate cross-target coupling. However, modeling such coupling raises difficulty: overly strong coupling can violate desired symmetries (e.g., the model should respect rigid motions applied to each pocket-ligand complex), or even constrain the joint variability (e.g., collapsing them to be related by a single rigid motion); whereas insufficient

coupling can yield poses that are mutually inconsistent with respect to a shared 2D molecular graph.

To address data scarcity, we derive a dual-target training set from BindingNet v2 [42] with paired ligand poses across targets, and use the full DualDiff benchmark [41] as an independent held-out test set, enabling principled training and evaluation of dual-target SBDD methods. To address modeling difficulty, we formalize the symmetries and expressiveness requirements for joint modeling. We then present **FUSEDIFF**, a conditional diffusion model that directly targets $p(G, X_1, X_2 \mid P_1, P_2)$ and satisfies these requirements by design. At its core, FUSEDIFF employs a message-passing backbone with *Dual-target Local Context Fusion (DLCF)*, which allows each ligand atom to fuse the local context from both pockets, to achieve appropriate cross-target coupling. Meanwhile, we explicitly model the bonds of the ligand to enhance topological consistency across both poses; without this, we consistently observe a failure mode in our pilot and ablation studies, where generated poses correspond to incompatible molecular graphs. We train and evaluate FUSEDIFF on the curated datasets and on a real-world dual-target pocket pair. In both settings, FUSEDIFF establishes the first benchmark for dual-target pose quality prior to docking-based pose search and achieves state-of-the-art performance under standard docking-based evaluation.

We summarize our main contributions as follows:

- To our knowledge, we introduce the first end-to-end conditional diffusion model for de novo dual-target SBDD that directly targets the density $p(G, X_1, X_2 \mid P_1, P_2)$ while satisfying all the desired symmetries and remaining expressive enough to model the joint density.
- We derive a dual-target SBDD training dataset with paired poses for the same ligand across targets, enabling principled training of joint ligand-pose generation.
- We propose a message-passing backbone with *Dual-target Local Context Fusion (DLCF)*, which enables suitable cross-target coupling and naturally generalizes to multi-target generative modeling.
- We establish the first benchmark for evaluating dual-target pose quality prior to docking-based pose search, and demonstrate state-of-the-art performance under standard docking-based metrics (Vina Dock) on both constructed and real-world pocket pairs.

2 Related Work

Structure-Based Drug Design. Recent SBDD methods formulate ligand design as 3D generative modeling conditioned on the pocket’s 3D structure [3, 29]. Early deep-learning approaches represented complexes on voxel grids [25, 32], which limits spatial resolution due to discretization and is not SE(3)-equivariant by construction. Continuous-coordinate methods leverage equivariant geometric GNNs [33] to construct ligands directly in 3D [22, 28]; however, autoregressive assembly is sequential and can be sampling-inefficient. Diffusion models [13] instead perform parallel denoising for one-shot generation [20, 34]; by jointly modeling continuous atom coordinates and discrete atom types, diffusion-based methods enable pose-consistent de novo design [12, 30, 31]. Recent evaluations further corroborate the strong performance of diffusion-based SBDD

on structure-conditioned generation [20]. Nevertheless, principled dual-target extensions of such models remain limited.

Protein–ligand complex datasets. Recent ML-based SBDD relies on protein-ligand complex datasets that provide 3D complex poses together with binding affinity data for supervised training and evaluation. While PDB archives experimentally determined macromolecular structures [4], curated resources such as PDBbind [37, 38] and Binding MOAD [1, 14] pair complex structures with literature-derived affinity measurements, and PDB-wide collections further expand affinity coverage [23]. Because experimentally derived datasets remain limited in scale and diversity, larger pose collections are built via modeling: docking-based datasets such as CrossDocked2020 primarily augment pose diversity for docking pipelines [8], whereas template-based datasets such as BindingNet v2 expand the coverage of experimentally annotated ligand–target pairs [42]. Dual-target resources are scarce; the DualDiff benchmark curates target pairs from synergistic drug combinations but provides distinct reference ligands per pocket, making it primarily an evaluation set [41]. Accordingly, we construct our training set from BindingNet v2 and reserve DualDiff dataset as an independent held-out evaluation set.

Dual-target ligand generation. Dual-target ligand generation aims to design single molecules that can simultaneously engage a given pair of biological targets. Most approaches generate molecules as SMILES or 2D graphs and may obtain docking poses via post-processing. Representative approaches include substructure-based generators that construct molecular graphs from learned or predefined fragments [16, 17], as well as target-pair-conditioned chemical language models fine-tuned on ligands associated with the target pair [15]. Optimization-driven methods further incorporate multi-objective rewards, ranging from adversarial/RL generators [24] to RL for polypharmacology [26]. Complementarily, Pareto-front search explores trade-offs via Pareto MCTS, either in general chemical space [39] or over synthesizable fragment libraries [6, 35]. Structure-based dual-target ligand generation is less explored: Zhou et al. [41] align two pockets in 3D and reprogram pretrained single-target diffusion models for dual-target sampling, producing a ligand together with a 3D conformation. In contrast, our work focuses on end-to-end joint generation of a shared molecular graph with two pocket-specific binding poses conditioned on the origin pocket pair.

3 Methodology

Having formulated dual-target SBDD as learning the conditional density $p(G, X_1, X_2 \mid P_1, P_2)$, we begin by specifying the problem setting and notation in Sec. 3.1. Sec. 3.2 introduces the datasets used for training and evaluation. We then elaborate on our proposed model FUSEDIFF in Sec. 3.3 and Sec. 3.4, followed by an analysis in Sec. 3.5 demonstrating that FUSEDIFF satisfies the desired requirements **R1–R4**.

3.1 Problem Definition

Given a pair of protein binding sites $(\mathcal{P}_1, \mathcal{P}_2)$, each pocket \mathcal{P}_k is represented as a set of $N_{\mathcal{P}_k}$ atoms $\mathcal{P}_k = \{(x_{\mathcal{P}_k}^{(i)}, v_{\mathcal{P}_k}^{(i)})\}_{i=1}^{N_{\mathcal{P}_k}}$, $k \in \{1, 2\}$ where $x_{\mathcal{P}_k}^{(i)} \in \mathbb{R}^3$ denotes the 3D coordinates of the i -th pocket

atom, and $v_{p_k}^{(i)} \in \{0, 1\}^{N_f}$ denotes its feature (e.g., element type and amino-acid type). Our goal is to generate a ligand molecular graph $\mathcal{G} = (\mathcal{V}, \mathcal{B})$, $\mathcal{V} = \{v_i\}_{i=1}^{N_M}$, $\mathcal{B} = \{b_{ij}\}_{i,j=1}^{N_M}$ together with its two target-specific binding conformations $\mathcal{X}_1 = \{x_{1,i}\}_{i=1}^{N_M}$ and $\mathcal{X}_2 = \{x_{2,i}\}_{i=1}^{N_M}$, conditioned on both pockets, where $x_{1,i} \in \mathbb{R}^3$ denotes the 3D coordinate of the i -th ligand atom in the \mathcal{P}_1 -specific binding conformation \mathcal{X}_1 (analogously for \mathcal{X}_2), $v_i \in \{0, 1\}^{N_v}$ denotes its atom type, and $b_{ij} \in \{0, 1\}^{N_b}$ denotes the bond type between atoms i and j , with N_v and N_b are the numbers of atom and bond types, respectively. In discussing density $p(G, X_1, X_2 | P_1, P_2)$, we use P_k , G , and X_k to denote both random variables and their corresponding realizations \mathcal{P}_k , \mathcal{G} , and \mathcal{X}_k , when there is no ambiguity. An ideal generative model should satisfy the following requirements:

Definition 3.1 (Requirements R1–R4). The learned $p(G, X_1, X_2 | P_1, P_2)$ satisfies **R1 permutation invariance** if $\forall \mathcal{G}, \mathcal{P}, \mathcal{P}', \mathcal{X}, \mathcal{X}'$, $p(\mathcal{G}, \mathcal{X}, \mathcal{X}' | \mathcal{P}, \mathcal{P}') = p(\mathcal{G}, \mathcal{X}', \mathcal{X} | \mathcal{P}', \mathcal{P})$. It satisfies **R2 SE(3) invariance** if $\forall g, g' \in \text{SE}(3)$, $p(\mathcal{G}, \mathcal{X}, \mathcal{X}' | \mathcal{P}, \mathcal{P}') = p(\mathcal{G}, \mathcal{T}_g \mathcal{X}, \mathcal{T}_{g'} \mathcal{X}' | \mathcal{T}_g \mathcal{P}, \mathcal{T}_{g'} \mathcal{P}')$. It satisfies **R3 Non-factorization** if $X_1 \not\perp X_2 | P_1, P_2, G$. It satisfies **R4 Non-restricted support** if its support is not restricted to $\{(X_1, X_2) : \exists g \in \text{SE}(3) \text{ s.t.}, X_1 = \mathcal{T}_g X_2\}$.

3.2 Dual-target Datasets

To support end-to-end learning of the density $p(G, X_1, X_2 | P_1, P_2)$, we require tuples in the form (G, X_1, X_2, P_1, P_2) . Since no public resource natively provides such tuples at scale, we derive the training data ourselves and use the DualDiff benchmark (DDF) for independent evaluation.

Training set BN2-DT. We build a dual-target training set from the high confidence subset of BindingNet v2 and term it *BindingNet v2–Dual-Target (BN2-DT)*. BindingNet v2 provides single-target complexes, which we view as entries (G, X, P) . A dual-target instance (G, X_1, X_2, P_1, P_2) is included if and only if two such entries share graph-isomorphic ligands (identical atom types and bond orders) and correspond to two distinct pockets/targets. Specifically, for two entries, namely (G_1, X_1, P_1) and (G_2, X_2, P_2) , if $G_1 \equiv G_2 \wedge P_1 \neq P_2$, we derive a dual-target tuple $(G = G_1 = G_2, X_1, X_2, P_1, P_2)$, where $P_1 \neq P_2$ denotes that the two pockets are distinct (Appendix A). We aggregate all eligible pairs with basic cleaning and deduplication, resulting in 58,058 dual-target training tuples. Full construction details and basic statistics are deferred to Appendix A.

Test set DDF. For an independent evaluation, we adopt the dual-target benchmark introduced by Zhou et al. [41], which curates *paired targets* from synergistic drug combinations and provides a *reference ligand* for each target. Consequently, each record can be treated as $(G_1, X_1, P_1, G_2, X_2, P_2)$, where typically $G_1 \neq G_2$ since the two pockets have distinct reference ligands. We refer to this benchmark as the *DUALDIFF test set (DDF)* and use it solely as an independent held-out test set.

3.3 Diffusion Models for dual-target SBDD

Overview of FUSEDIFF. As shown in Fig. 1, FUSEDIFF is a diffusion model that consists of a fixed forward (diffusion) process and a trainable reverse (denoising) process. For notational convenience, we denote $M = (G, X_1, X_2)$ and $P = (P_1, P_2)$. Then the conditional

density estimated by FUSEDIFF is expressed as $p_\theta(M^{(0)} | P) = \int p_\theta(M^{(0:T)} | P) dM^{(1:T)}$, where $M^{(t)}$ for $t = 1, \dots, T$ is a sequence of latent variables with the same dimensionality as the data $M^{(0)}$. The forward process gradually corrupts data until reaching a stationary base distribution. The reverse process performs step-wise denoising with a denoiser, recovering samples back towards the data distribution.

To enhance *topology consistency*: generating different X_1 and X_2 while keeping both consistent with the generated G , FUSEDIFF generates G —including both atom types V and bond types B as defined in Sec. 3.1—together with (X_1, X_2) , thus enforcing a single shared molecular graph during joint generation. Without explicitly generating B , bonds are inferred post hoc for each pose independently. In our ablation study (Sec. 4.3), removing explicit bond-type modeling breaks topology consistency and prevents generating plausible samples.

The diffusion denoiser takes the noisy variables $M^{(t)} = (V^{(t)}, B^{(t)}, X_1^{(t)}, X_2^{(t)})$, the timestep t , and the pair of conditioning pockets P , as input, and predicts all components of $M^{(0)}$ jointly. To achieve suitable cross-target coupling, our denoiser relies on Dual-target Local Context Fusion (DLCF) elaborated in Sec. 3.4.

Diffusion Process. Following the convention in single-target SBDD methods [12], we apply Gaussian diffusion to the continuous coordinates (X_1, X_2) and categorical diffusion for discrete graph attributes $G = (V, B)$, including atom and bond types. The t -step forward marginals factorize as:

$$q(M^{(t)} | M^{(0)}) = q(G^{(t)} | G^{(0)}) q(X_1^{(t)} | X_1^{(0)}) q(X_2^{(t)} | X_2^{(0)}), \quad (1)$$

where the noise is injected independently for each component $(X_1, X_2, \text{ and } G)$, and within each component independently across atoms and edges. Specifically, the categorical transition is defined by $q(G^{(t)} | G^{(0)}) = q(V^{(t)} | V^{(0)}) q(B^{(t)} | B^{(0)})$ with $q(V^{(t)} | V^{(0)}) = \prod_{i=1}^n \mathcal{C}(v_i^{(t)} | \bar{\alpha}_t v_i^{(0)} + (1 - \bar{\alpha}_t) \text{Unif}([N_v]))$ and $q(B^{(t)} | B^{(0)}) = \prod_{i < j} \mathcal{C}(b_{ij}^{(t)} | \bar{\alpha}_t b_{ij}^{(0)} + (1 - \bar{\alpha}_t) \mathbb{1}_{\text{none-type}})$, where $\text{Unif}([N_v])$ is the uniform categorical over $[N_v] = \{1, \dots, N_v\}$, and $\mathbb{1}_{\text{none-type}}$ is the one-hot categorical concentrated on the “none-type”. For $k \in \{1, 2\}$, we apply the i.i.d. Gaussian noise per atom: $q(X_k^{(t)} | X_k^{(0)}) = \prod_{i=1}^n \mathcal{N}(x_{k,i}^{(t)} | \sqrt{\bar{\alpha}_t} x_{k,i}^{(0)}, (1 - \bar{\alpha}_t) \mathbf{I})$. Here $\{\beta_t\}_{t=1}^T$ is a predefined noise scheduler, and we denote $\alpha_t = 1 - \beta_t$ and $\bar{\alpha}_t = \prod_{s=1}^t \alpha_s$ for the cumulative signal coefficient. We follow Peng et al. [27] for the noise schedule $\{\bar{\alpha}_t\}_{t=1}^T$, including a bond-first corruption that quickly absorbs bonds to the *none-type*. As $t \rightarrow T$, the forward marginals approach a simple terminal prior, which we take as the base distribution to initialize reverse sampling: $p_{\text{base}}(M^{(T)} | P) = \mathcal{N}(X_1^{(T)}; 0, \mathbf{I}) \mathcal{N}(X_2^{(T)}; 0, \mathbf{I}) \mathcal{C}(V^{(T)}; \text{Unif}(N_v)) \mathcal{C}(B^{(T)}; \mathbb{1}_{\text{none-type}})$.

Parameterization of the denoising process. Starting from the base prior $p_{\text{base}}(M^{(T)} | P)$, we define a Markov chain $p_\theta(M^{(0:T)} | P) = p_{\text{base}}(M^{(T)} | P) \prod_{t=1}^T p_\theta(M^{(t-1)} | M^{(t)}, P)$. Following the factorization of the diffusion process (Eq. 1), we factorize the reverse transition as $p_\theta(M^{(t-1)} | M^{(t)}, P) = \left(\prod_{k=1}^2 p_\theta(X_k^{(t-1)} | M^{(t)}, P) \right) p_\theta(V^{(t-1)} | M^{(t)}, P) p_\theta(B^{(t-1)} | M^{(t)}, P)$, where all these terms are approximated by substituting the denoised components into the

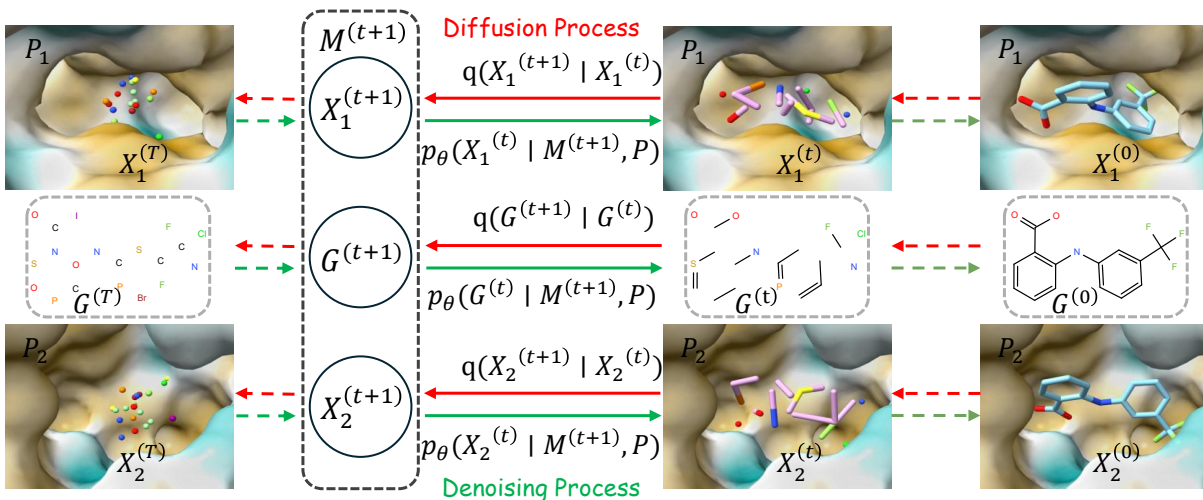


Figure 1: Overview of FUSEDIFF. FUSEDIFF defines a conditional diffusion model over $M = (G, X_1, X_2)$ given a pocket pair $P = (P_1, P_2)$, where the two target-specific complexes share the same molecular graph G while maintaining separate poses in P_1 and P_2 . A fixed forward (diffusion) process q (red arrows) corrupts $(G^{(0)}, X_1^{(0)}, X_2^{(0)})$ into $(G^{(T)}, X_1^{(T)}, X_2^{(T)})$ for training. For generation, the learned reverse (denoising) process p_θ (green arrows) starts from $M^{(T)} \sim p_{\text{base}}(M^{(T)} | P)$ and iteratively samples $M^{(t-1)}$ using a denoiser f_θ . At step t , f_θ takes $(G^{(t)}, X_1^{(t)}, X_2^{(t)})$, t , and P as input and predicts $(\widehat{X}_1^{(0)}, \widehat{X}_2^{(0)}, \widehat{V}^{(0)}, \widehat{B}^{(0)})$ to parameterize the reverse transition.

one-step posteriors [13, 27]: $p_\theta(X_k^{(t-1)} | M^{(t)}, P) = q(X_k^{(t-1)} | X_k^{(t)}, \widehat{X}_k^{(0)})$, $p_\theta(V^{(t-1)} | M^{(t)}, P) = q(V^{(t-1)} | V^{(t)}, \widehat{V}^{(0)})$, and $p_\theta(B^{(t-1)} | M^{(t)}, P) = q(B^{(t-1)} | B^{(t)}, \widehat{B}^{(0)})$. All these denoised components are jointly predicted by a single denoiser f_θ :

$$(\widehat{X}_1^{(0)}, \widehat{X}_2^{(0)}, \widehat{V}^{(0)}, \widehat{B}^{(0)}) = f_\theta(M^{(t)}, t, P). \quad (2)$$

Optimization. At each training iteration, we sample a training tuple (M, P) and draw $t \sim \text{Unif}(\{1, \dots, T\})$. We then obtain $M^{(t)} \sim q(M^{(t)} | M^{(0)} = M)$ by Eq. 1, and make predictions by Eq. 2. The clean sample and these predictions together define a weighted denoising objective to optimize f_θ :

$$\mathcal{L}_{t-1} = \lambda \left(\mathcal{L}_{t-1}^{\text{pos}_1} + \mathcal{L}_{t-1}^{\text{pos}_2} \right) + \lambda_v \mathcal{L}_{t-1}^{\text{a-type}} + \lambda_b \mathcal{L}_{t-1}^{\text{b-type}} + \lambda_{bl} \mathcal{L}_{t-1}^{\text{b-len}}.$$

Here $\mathcal{L}_{t-1}^{\text{pos}_k}$ is the MSE between $\widehat{X}_k^{(0)}$ and $X_k^{(0)}$. $\mathcal{L}_{t-1}^{\text{a-type}}$ and $\mathcal{L}_{t-1}^{\text{b-type}}$ are KL divergences that match the predicted one-step posteriors parameterized by $\widehat{V}^{(0)}$ and $\widehat{B}^{(0)}$ to its counterpart induced by ground-truth $V^{(0)}$ and $B^{(0)}$. We additionally include a MSE loss $\mathcal{L}_{t-1}^{\text{b-len}}$ for bond-length over bonded pairs, regressing interatomic distances to the ground truth to enforce plausible covalent lengths. The weights $\lambda, \lambda_v, \lambda_b, \lambda_{bl}$ are nonnegative hyperparameters controlling the relative contributions of each term.

3.4 Dual-target Local Context Fusion (DLCF)

We parameterize the denoiser f_θ as an L -layer MPNN [10] that is SE(3)-equivariant under independent rigid motions of each pocket-ligand complex. To predict the reverse transition in Eq. 2, f_θ takes the current noisy complexes at denoising step t as input. In each layer ℓ , f_θ dynamically constructs two pocket-ligand point-cloud graphs and fuses them into a single augmented graph, then updates

node/edge representations via message passing on the augmented graph (Eq. 3–6), thereby injecting local context from both pockets into shared ligand atom/bond embeddings, and finally updates ligand coordinates in the two point-cloud graphs separately (Eq. 7), as illustrated in Fig. 2.

3.4.1 Dual-target graph setup. At the ℓ -th MPNN layer ($\ell \in \{1, \dots, L\}$), we denote the current ligand-pocket complexes by $R_k^{(\ell)} := \{\mathbf{r}_{k,u}^{(\ell)}\}_{u \in V}$ for $k \in \{1, 2\}$. Here, the subscript u indexes the atom, and thus $\mathbf{r}_{k,u}^{(\ell)} \in \mathbb{R}^3$ denotes the coordinate of the atom u in the k -th complex at layer ℓ . When u corresponds to a pocket’s atom, $\mathbf{r}_{k,u}^{(\ell)}$ always takes value from the condition P_k across the layers. When u corresponds to the ligand’s atom, we initialize $\mathbf{r}_{k,u}^{(\ell)}$ by the input noisy coordinate $X_{k,u}^{(\ell)}$ and update it across the L layers. We construct a protein-ligand point-cloud graph $G_k^{(\ell)}$. The nodes of $G_k^{(\ell)}$ consist of ligand atoms and pocket atoms in P_k . Within $G_k^{(\ell)}$, ligand nodes are fully connected, while all remaining edges are constructed by 3D k -nearest neighbors in terms of $R_k^{(\ell)}$ following Guan et al. [12]. We use $\mathcal{N}_k^{(\ell)}(u)$ to denote the neighbors of node u in $G_k^{(\ell)}$.

We then build an *augmented graph* $G_{\text{aug}}^{(\ell)}$ by fusing the local neighborhoods of $G_1^{(\ell)}$ and $G_2^{(\ell)}$ for dual-target message passing. Since $G_1^{(\ell)}$ and $G_2^{(\ell)}$ share the same ligand identities but have target-specific coordinates, we deduplicate ligand nodes and define the node set of $G_{\text{aug}}^{(\ell)}$ as $V \cup P_1 \cup P_2$. Here, V, P_1 , and P_2 are overloaded to denote the disjoint node subsets corresponding to the ligand atoms and the pocket atoms from the two targets, respectively, when there is no ambiguity. In $G_{\text{aug}}^{(\ell)}$, ligand nodes remain fully connected and all intra-pocket edges are preserved. Crucially, for each ligand node $u \in$

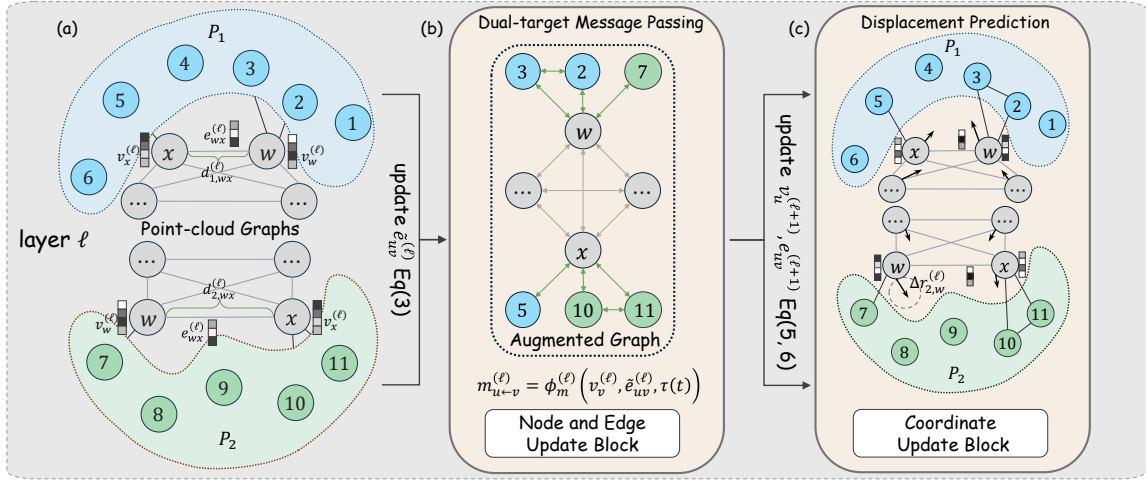


Figure 2: Dual-target Local Context Fusion (DLCF) within one denoising layer. (a) Two pocket–ligand point-cloud graphs for P_1 and P_2 , each containing a fully-connected ligand subgraph. (b) The *augmented graph* induced from the two point-cloud graphs, on which dual-target message passing updates node/edge embeddings. (c) Coordinate update block that *separately* updates ligand node coordinates in the two point-cloud graphs (with pocket atoms fixed).

V , its pocket-atom neighbors are inherited from *both* $G_1^{(\ell)}$ and $G_2^{(\ell)}$. Formally, let $\mathcal{N}^{(\ell)}(u)$ denote the neighbors of u in $G_{\text{aug}}^{(\ell)}$. Accordingly, for a pocket node $u \in P_k$, $\mathcal{N}^{(\ell)}(u) = \mathcal{N}_k^{(\ell)}(u)$; for a ligand node $u \in V$, $\mathcal{N}^{(\ell)}(u) = \mathcal{N}_1^{(\ell)}(u) \cup \mathcal{N}_2^{(\ell)}(u)$ after deduplicating ligand nodes. An example of this fusion procedure is illustrated in Fig. 2 ((a)→(b)).

The l -th layer MPNN will perform message passing on $G_{\text{aug}}^{(\ell)}$. We denote current node and edge representations by $v_u^{(\ell)} \in \mathbb{R}^{d_v}$ and $e_{uv}^{(\ell)} \in \mathbb{R}^{d_e}$, respectively, with $\ell = 1$ initialized from input atom/bond type embeddings together with the timestep embedding $\tau(t)$.

3.4.2 Dual-target message-passing. For each edge (u, v) in $G_{\text{aug}}^{(\ell)}$, we first compute a distance-aware edge embedding $\tilde{e}_{uv}^{(\ell)}$ by injecting the inter-atomic distance $d_{k,uv}^{(\ell)} = \|\mathbf{r}_{k,u}^{(\ell)} - \mathbf{r}_{k,v}^{(\ell)}\|_2$ into the edge representation $e_{uv}^{(\ell)}$:

$$\tilde{e}_{uv}^{(\ell)} = \begin{cases} \phi_{d,v}^{(\ell)}(e_{uv}^{(\ell)}, s_{uv}^{(\ell)}, \delta_{uv}^{(\ell)}), & u, v \in V, \\ \phi_{d,p}^{(\ell)}(e_{uv}^{(\ell)}, d_{k,uv}^{(\ell)}), & u \in P_k \text{ or } v \in P_k. \end{cases} \quad (3)$$

Here, note that $G_{\text{aug}}^{(\ell)}$ contains no edges between P_1 and P_2 , hence k is uniquely determined in the second case. Meanwhile, by letting $s_{uv}^{(\ell)} = d_{1,uv}^{(\ell)} + d_{2,uv}^{(\ell)}$ and $\delta_{uv}^{(\ell)} = |d_{1,uv}^{(\ell)} - d_{2,uv}^{(\ell)}|$, the formulation in the first case is invariant to swapping the two targets. Distance-aware edge embeddings encode the required geometric cues, allowing us to perform node/edge updates on $G_{\text{aug}}^{(\ell)}$ using only scalar distances without explicit 3D relative displacement vectors. Then, we compute a directed message from node v to node u via:

$$m_{u \leftarrow v}^{(\ell)} = \phi_m^{(\ell)}(v_v^{(\ell)}, \tilde{e}_{uv}^{(\ell)}, \tau(t)). \quad (4)$$

The above transformations $\phi_{d,v}^{(\ell)}$, $\phi_{d,p}^{(\ell)}$, and $\phi_m^{(\ell)}$ are neural networks composed of different multilayer perceptrons (MLPs). Finally, we update node representations $v_u^{(\ell+1)}$ by aggregating messages from

$\mathcal{N}^{(\ell)}(u)$:

$$v_u^{(\ell+1)} = \text{Linear}(v_u^{(\ell)}) + \sum_{v \in \mathcal{N}^{(\ell)}(u)} m_{u \leftarrow v}^{(\ell)}. \quad (5)$$

This design allows each ligand node to incorporate pocket-local context from both targets, since $\mathcal{N}^{(\ell)}(u)$ contains atoms from both pockets. Similarly, edge representations $e_{uv}^{(\ell)}$ are updated via message passing according to:

$$e_{uv}^{(\ell+1)} = \sum_{\xi \in \{u,v,e\}} \text{Linear}_{\xi}(h_{\xi}^{(\ell)}) + \sum_{s \in \{u,v\}} \sum_{w \in \mathcal{N}^{(\ell)}(s)} m_{s \leftarrow w}^{(\ell)}, \quad (6)$$

where $h_u^{(\ell)} = v_u^{(\ell)}$, $h_v^{(\ell)} = v_v^{(\ell)}$, $h_e^{(\ell)} = e_{uv}^{(\ell)}$.

Unlike node/edge representation updates that are performed on $G_{\text{aug}}^{(\ell)}$, coordinate updates are performed separately in $G_k^{(\ell)}$, $k \in \{1, 2\}$. Moreover, we update only the coordinates of the ligand atoms while keeping the coordinates of the pocket atoms fixed. Specifically, for each $G_k^{(\ell)}$, we predict an SE(3)-equivariant displacement for every ligand node using the just-updated node/edge embeddings: $\mathbf{r}_{k,u}^{(\ell+1)} = \mathbf{r}_{k,u}^{(\ell)} + \Delta \mathbf{r}_{k,u}^{(\ell)}$, where $\Delta \mathbf{r}_{k,u}^{(\ell)}$ is calculated as follows:

$$\Delta \mathbf{r}_{k,u}^{(\ell)} = \sum_{w \in \mathcal{N}_k^{(\ell)}(u)} \phi_r^{(\ell)}(v_u^{(\ell+1)}, v_w^{(\ell+1)}, \tilde{e}_{uw}^{(\ell+1)}, \tau(t)) \frac{\mathbf{r}_{k,u}^{(\ell)} - \mathbf{r}_{k,w}^{(\ell)}}{d_{k,uw}^{(\ell)}}. \quad (7)$$

The update is SE(3)-equivariant because $\phi_r^{(\ell)}$ uses only invariant inputs and scales a relative vector.

Importantly, updating coordinates separately on $G_k^{(\ell)}$ does not imply single-pocket conditioning or a two-stage design. The displacement field depends on the newly updated node and edge representations that have already fused local contexts from both pockets.

Extension to multi-target. The above design extends naturally to K targets by building K pocket–ligand point-cloud graphs. We

fuse them into an augmented graph by starting from the fully-connected ligand subgraph, attaching to each ligand node u its pocket-atom neighbors from all K point-cloud graphs, and retaining all intra-pocket edges. Node/edge embeddings are updated on this augmented graph as before, while ligand coordinates are updated independently in each point-cloud graph.

3.5 Analysis

As we have identified four requirements **R1–R4** for generative modeling of $p(G, X_1, X_2 | P_1, P_2)$ in Def. 3.1, we check whether existing methods and our proposed FUSEDIFF satisfy them. Benefited from their decomposition of the target distribution and the adoption of geometric GNNs, most existing methods satisfy **R1&R2**. However, the benefit is not free: The molecule-then-poses strategy [36] breaks **R3**; and the pocket alignment preprocessing [41] breaks **R4**.

PROPOSITION 3.2. *FUSEDIFF satisfies R1–R4.*

Due to the limited space, we defer the proof to Appendix B.

4 Experiment

Our experiments evaluate the chemical properties, binding affinity proxies and dual-target binding compatibility of generated ligands, verify the necessity of our key design through ablations, and further demonstrate real-world utility in an Alzheimer’s disease polypharmacology setting by designing dual-kinase inhibitors for **GSK3 β** and **JNK3**.

4.1 Experimental Setup

Dataset. We train FUSEDIFF on our derived dual-target training set BN2-DT and evaluate on DDF (Sec. 3.2). For controlled comparison, we train a TARGETDIFF checkpoint on BindingNet v2 and use it as the pretrained single-target model for TARGETDIFF, DUALDIFF, and COMPDIFF. This controls for differences in single-target pretraining data, so the results reflect the dual-target modeling design rather than the choice of pretraining dataset. Appendix C shows that the BindingNet v2 checkpoint performs on par with the official CrossDocked2020 checkpoint on DDF, supporting its use as a common pretrained backbone for fair benchmarking.

Baselines. We compare FUSEDIFF with the reference ligands in the test set and the ligands generated by several baselines. TARGETDIFF [12] is a diffusion-based method originally proposed for single-target de novo SBDD. LINKERNET [11] is a diffusion-based model for co-designing molecular fragment poses and the linker. Following Zhou et al. [41], we apply TARGETDIFF and repurpose LINKERNET to the dual-target setting. DUALDIFF and COMPDIFF [41] are dual-target sampling methods that reprogram pretrained single-target diffusion models by aligning two binding pockets. We exclude search-based methods (e.g., COMBIMOTS) that rely on MCTS with iterative oracle/docking evaluations over an external building-block space, as their compute-budgeted search setting is not directly comparable to our learned generative baselines.

Metrics. We evaluate generated ligands from two perspectives: **molecular properties** and **protein–ligand interactions**.

molecular properties. We adopt widely used metrics from prior work [12, 20] and report (i) **QED** (\uparrow) [5] for drug-likeness;

Table 1: Molecular property statistics of generated ligands and reference ligands (Avg.). (\uparrow) indicates higher is better. Top 2 results (excluding Ref.) are highlighted with bold text and underlined text, respectively.

| Methods | Metrics | | | | |
|-----------------|-------------------|------------------|--------------------|------|--------------------|
| | QED(\uparrow) | SA(\uparrow) | Div.(\uparrow) | logP | LPSK(\uparrow) |
| Ref. | 0.51 | 0.77 | 0.74 | 2.89 | 4.50 |
| TARGETDIFF | 0.54 | 0.55 | 0.67 | 2.32 | 4.69 |
| COMPDIFF | 0.59 | 0.57 | 0.69 | 3.48 | 4.74 |
| DUALDIFF | 0.59 | 0.58 | 0.69 | 3.54 | <u>4.88</u> |
| LINKERNET | <u>0.61</u> | <u>0.61</u> | 0.29 | 3.21 | 4.71 |
| FUSEDIFF | 0.64 | 0.68 | <u>0.68</u> | 2.47 | 4.92 |

(ii) **SA** (\uparrow) [7] for synthetic accessibility; (iii) **Diversity (Div.)** (\uparrow) as the average pairwise Tanimoto distance between molecular fingerprints; (iv) **logP** measuring lipophilicity via the octanol–water partition coefficient (typically $[-0.4, 5.6]$ for drug-like compounds); and (v) **LPSK** (\uparrow), the number of satisfied criteria in Lipinski’s Rule-of-Five [21], averaged over generated molecules.

interactions. For structure-based evaluation of protein–ligand interactions, we report widely used binding-affinity proxies computed by AutoDock Vina: (i) **Vina Score** (\downarrow), the affinity of a given pose in the target pocket (scoring the given pose without optimization); (ii) **Vina Min** (\downarrow), the affinity after local optimization (energy minimization) in the pocket; (iii) **Vina Dock** (\downarrow), the best affinity after conformational search in the pocket. Accordingly, **Vina Score** and **Vina Min** are both highly dependent on the input pose and evaluate poses prior to docking-based pose search, whereas **Vina Dock** is a docking-based score that performs global conformational search. As Vina scores are biased by ligand size (larger molecules tend to score lower) [9, 20], we additionally report (iv) **LBE** = $\frac{E_{\text{vina}}}{N_{\text{lig}}}$ (\downarrow) [20], measuring per-atom binding contribution to reduce size effects. For the dual-target setting, we further report (v) **Max Vina Dock** (\downarrow), the maximum of the two **Vina Dock** scores against P_1 and P_2 , and (vi) **Dual High Affinity** (\uparrow), the fraction of molecules whose affinities on both targets surpass the reference ligand, reflecting dual-target compatibility [41].

Evaluation protocol. We evaluate on the DDF benchmark containing 12,917 dual-target instances, each specifying a pocket pair (P_1, P_2) . For each instance, we sample $K=10$ ligands by each method conditioned on (P_1, P_2) , and report the overall mean (Avg.) and median (Med.) over all generated ligands. For Vina Score, we additionally report the trimmed mean (T-Avg) by discarding the top and bottom 5% samples to mitigate outliers.

4.2 Results and Analysis

Table 1 summarizes molecular property statistics of the generated ligands. FUSEDIFF achieves the best QED, SA, and LPSK among all methods, while achieving diversity on par with the top-performing baselines; ligands generated by FUSEDIFF also have logP within the drug-like range ($[-0.4, 5.6]$).

We also quantify the generation validity of jointly generating two target-specific poses that correspond to the same molecular

Table 2: Dual-pose quality before docking-based pose search. “-” denotes not applicable (N/A) when a method does not produce target-specific binding poses for the corresponding pocket, and “OOR” denotes out-of-range values caused by extreme/invalid poses that fall outside the reported scale.

| Methods | Metrics | | | | | | | | | |
|-----------------|-------------------|--------|-------|-------------------|--------|-------|-----------------|-------|-----------------|-------|
| | P1-Vina Score (↓) | | | P2-Vina Score (↓) | | | P1-Vina Min (↓) | | P2-Vina Min (↓) | |
| | Avg. | T-Avg. | Med. | Avg. | T-Avg. | Med. | Avg. | Med. | Avg. | Med. |
| Ref. | -7.92 | -7.97 | -7.83 | -7.86 | -7.92 | -7.92 | -8.02 | -7.89 | -7.93 | -7.96 |
| TARGETDIFF | -6.36 | -7.03 | -7.26 | - | - | - | -7.78 | -7.95 | - | - |
| COMPDIFF | OOR | -1.68 | -3.46 | - | - | - | OOR | -6.26 | - | - |
| DUALDIFF | OOR | -2.47 | -3.63 | - | - | - | OOR | -6.27 | - | - |
| FUSEDIFF | -5.99 | -6.39 | -6.39 | -5.81 | -6.35 | -6.42 | -7.47 | -7.57 | -7.50 | -7.52 |

Table 3: Docking-based interaction evaluation and dual-target compatibility. Top 2 results (excluding Ref.) are highlighted with bold text and underlined text, respectively.

| Methods | Metrics | | | | | | | | | |
|-----------------|------------------|--------------|--------------|------------------|--------------|--------------|-------------------|--------------|--------------------|--------------|
| | P1-Vina Dock (↓) | | | P2-Vina Dock (↓) | | | Max Vina Dock (↓) | | Dual High Aff. (↑) | |
| | Avg. | Med. | LBE | Avg. | Med. | LBE | Avg. | Med. | Avg. | Med. |
| Ref. | -8.23 | -7.98 | -0.38 | -8.14 | -8.23 | -0.37 | -6.15 | -6.73 | - | - |
| TARGETDIFF | <u>-8.95</u> | <u>-8.86</u> | -0.35 | -7.14 | -7.99 | -0.28 | -6.88 | -7.36 | 31.1% | 23.4% |
| COMPDIFF | -8.75 | -8.79 | <u>-0.36</u> | <u>-8.73</u> | -8.65 | <u>-0.36</u> | -7.92 | -7.98 | 39.8% | 33.0% |
| DUALDIFF | -8.80 | -8.82 | -0.37 | -8.72 | <u>-8.78</u> | -0.37 | <u>-7.99</u> | <u>-8.09</u> | 40.5% | 33.4% |
| LINKERNET | -8.34 | -8.43 | -0.35 | -8.30 | -8.42 | -0.34 | -7.65 | -7.79 | 38.1% | 30.5% |
| FUSEDIFF | -9.11 | -9.13 | -0.37 | -9.16 | -9.12 | -0.37 | -8.37 | -8.43 | 49.2% | 40.9% |

graph, which is a more stringent criterion in the dual-target setting. We define **Dual-Validity** as the percentage of samples for which OpenBabel can assemble a chemically valid molecule from both generated poses given a single atom/bond assignment (i.e., both (G, X_1) and (G, X_2) are valid). FUSEDIFF achieves **61%** Dual-Validity. This criterion is not applicable to prior methods, as they cannot directly generate a molecule with two target-specific poses. In contrast, FUSEDIFF directly generates two binding poses and assesses their joint assembly validity, thereby establishing **Dual-Validity** as a standardized measure for this criterion.

Table 2 reports pose-dependent **Vina Score** and **Vina Min**, which are only defined for methods that explicitly output a pocket-specific binding pose prior to docking-based pose search. We denote N/A (“-”) when such a pose is unavailable (no pose output) or lies outside the Vina scoring box (out-of-box), and use **OOR** when a pose is available but yields extremely unfavorable scores. LINKERNET is not target-aware and does not generate binding poses, so these scores are not applicable (N/A) for both pockets. TARGETDIFF generates ligands/poses conditioned on P_1 , and the resulting conformations are typically out-of-box for P_2 , making P_2 pose-dependent scoring N/A. Similarly, DUALDIFF/COMPDIFF sample a single conformation from the composed conditional $p(G, X | P_1, \mathcal{T}P_2)$, which concentrates near P_1 in the aligned frame; therefore, pose-dependent scoring against the original P_2 prior to search is N/A. In contrast, FUSEDIFF directly generates a single molecular graph with two pocket-specific poses (X_1, X_2) , establishing the first benchmark for evaluating dual-target pose quality before docking-based search while achieving competitive Vina scores on both pockets.

For docking-based metrics reported in Table 3, our method achieves state-of-the-art results on this test set, obtaining the best Vina Dock on both P_1 and P_2 , as well as the lowest Max Vina Dock and the highest Dual High Affinity. These results indicate that, despite strictly enforcing atom/bond-type consistency and jointly generating two pocket-specific conformations, our model can still produce high-quality dual-target ligands with strong and balanced binding across both targets.

4.3 Ablation Studies

We conduct ablations on FUSEDIFF targeting two components that are crucial for ensuring *topology consistency* and *symmetry preservation* (Sec. 3.3): *bond generative modeling* and *DLCF*. Unlike conventional ablations that lead to gradual performance drops, removing either component breaks the consistency constraints required by the dual-target setting and causes a near-complete collapse in assembly validity. Detailed ablation setups, failure modes, and quantitative results are deferred to Appendix D.

4.4 Study on a Real-world Case

To evaluate the capability of FUSEDIFF in exploring promising ligands for realistic dual-target drug design scenarios, we establish a dual-target inhibitor design task on two kinases related to Alzheimer’s Disease (AD): glycogen synthase kinase-3 beta (GSK3 β , PDB: 6Y9S) and c-Jun N-terminal kinase 3 (JNK3, PDB: 4WHZ). This target pair has been widely used as a representative real-world test case in prior dual-target molecular design studies[6, 35], and

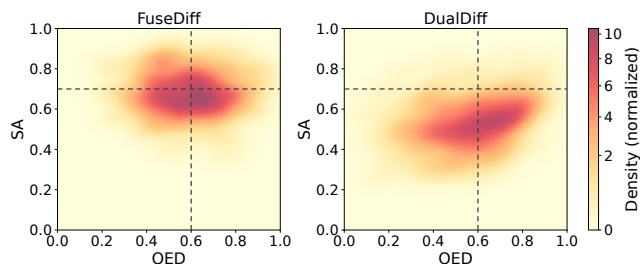


Figure 3: QED-SA density of filtered molecules (LPSK = 5, $\log P \in [-0.4, 5.6]$). KDE heatmaps show QED (x-axis) versus SA (y-axis) for FUSEDIFF (left) and DUALDIFF (right). The upper-right region corresponds to DL (QED > 0.6, SA > 0.7), where FUSEDIFF shows higher density, consistent with its larger DL yield (78 vs. 15).

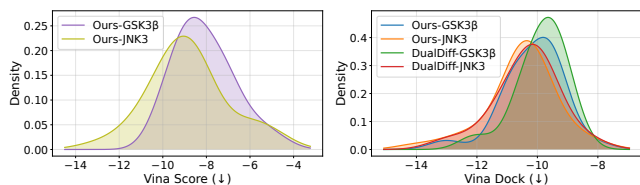


Figure 4: Vina Score and Vina Dock distributions on GSK3 β and JNK3. Left: FUSEDIFF Vina Score on generated poses. Right: Vina Dock after Vina conformational search for FUSEDIFF and DUALDIFF.

designing inhibitors that simultaneously act on GSK3 β and JNK3 is regarded as a potential polypharmacology strategy for AD [19].

Drug-like molecules. We sample 1000 molecules for each method and define DL (drug-like) as QED > 0.6, SA > 0.7, $\log P \in [-0.4, 5.6]$, and LPSK = 5. Under this unified criterion, FUSEDIFF yields substantially more DL molecules than DUALDIFF (78 vs. 15). Fig. 3 shows the QED-SA KDE heatmaps of molecules with LPSK = 5 and $\log P \in [-0.4, 5.6]$ generated by FUSEDIFF and DUALDIFF; FUSEDIFF assigns substantially more probability mass to the DL region (QED > 0.6, SA > 0.7).

Interaction. For the DL molecules generated by FUSEDIFF and DUALDIFF, we evaluate structure-based binding affinity proxies on both pockets using AutoDock Vina and summarize the score distributions with KDE (Fig. 4). Specifically, the left panel reports Vina Score of FUSEDIFF evaluated on the generated poses (without conformational optimization or search), while the right panel reports Vina Dock after Vina docking search for both methods on both pockets. Overall, FUSEDIFF achieves Vina Score comparable to the Vina Dock of DUALDIFF, and further yields consistently better Vina Dock distributions than DUALDIFF on both pockets.

Visualization. We curate single-target active molecules from ChEMBL for each pocket (GSK3 β : 2128; JNK3: 791) and identify 3 graph-isomorphic molecules shared by both sets (Appendix E), which we treat as reference dual-target ligands. Fig. 5 provides a qualitative comparison in the two pockets: the left column shows a reference ligand with its target-specific binding poses obtained via

Vina pose search, while the middle and right columns show two FUSEDIFF samples, including both the generated ligands and their binding poses sampled by the model without any optimization.

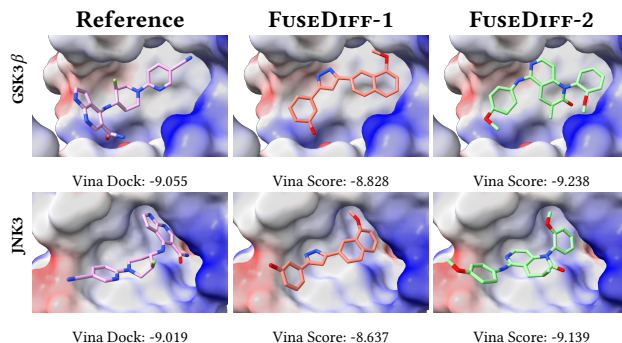


Figure 5: Qualitative visualization in two pockets. Top: GSK3 β ; bottom: JNK3. Left: a reference dual-target ligand with poses obtained by Vina pose search. Middle/Right: two FUSEDIFF samples.

5 Conclusion

To our knowledge, FUSEDIFF is the first symmetry-preserving diffusion model for end-to-end dual-target SBDD that jointly generates a shared ligand graph and its two pocket-specific binding poses. FUSEDIFF achieves this by Dual-target Local Context Fusion (DLCF) and explicit bond modeling. Trained on our constructed BN2-DT dataset, FUSEDIFF enables the first systematic pre-docking evaluation of dual-pose quality and achieves state-of-the-art docking performance on the DualDiff benchmark and a real GSK3 β -JNK3 case. More broadly, our study suggests a practical design principle for multi-target SBDD with the potential to accelerate polypharmacology-oriented drug discovery.

References

- [1] Aqeel Ahmed, Richard D. Smith, Jordan J. Clark, Jr Dunbar, James B., and Heather A. Carlson. 2014. Recent improvements to Binding MOAD: a resource for protein-ligand binding affinities and structures. *Nucleic Acids Research* 43, D1 (11 2014), D465–D469.
- [2] Amy C. Anderson. 2003. The Process of Structure-Based Drug Design. *Chemistry & Biology* 10, 9 (01 Sep 2003), 787–797.
- [3] Qifeng Bai, Tingyang Xu, Junzhou Huang, and Horacio Pérez-Sánchez. 2024. Geometric deep learning methods and applications in 3D structure-based drug design. *Drug Discovery Today* 29, 7 (2024), 104024.
- [4] Helen M. Berman, John Westbrook, Zukang Feng, Gary Gilliland, T. N. Bhat, Helge Weissig, Ilya N. Shindyalov, and Philip E. Bourne. 2000. The Protein Data Bank. *Nucleic Acids Research* 28, 1 (01 2000), 235–242.
- [5] G. Richard Bickerton, Gaia V. Paolini, Jérémy Besnard, Sorel Muresan, and Andrew L. Hopkins. 2012. Quantifying the chemical beauty of drugs. *Nature Chemistry* 4, 2 (2012), 90–98.
- [6] Sheng Chen, Junjie Xie, Renlong Ye, David Daqiang Xu, and Yuedong Yang. 2024. Structure-aware dual-target drug design through collaborative learning of pharmacophore combination and molecular simulation. *Chem. Sci.* 15 (2024), 10366–10380. Issue 27.
- [7] Peter Ertl and Ansgar Schuffenhauer. 2009. Estimation of synthetic accessibility score of drug-like molecules based on molecular complexity and fragment contributions. *Journal of Cheminformatics* 1, 1 (2009), 8.
- [8] Paul G. Francoeur, Tomohide Masuda, Jocelyn Sunseri, Andrew Jia, Richard B. Iovanisci, Ian Snyder, and David R. Koes. 2020. Three-Dimensional Convolutional Neural Networks and a Cross-Docked Data Set for Structure-Based Drug Design. *J. Chem. Inf. Model.* 60, 9 (2020), 4200–4215.
- [9] Bowen Gao, Haichuan Tan, Yanwen Huang, Minsi Ren, Xiao Huang, Wei-Ying Ma, Ya-Qin Zhang, and Yanyan Lan. 2025. Reframing Structure-Based Drug Design Model Evaluation via Metrics Correlated to Practical Needs. In *The Thirteenth International Conference on Learning Representations*.
- [10] Justin Gilmer, Samuel S. Schoenholz, Patrick F. Riley, Oriol Vinyals, and George E. Dahl. 2017. Neural Message Passing for Quantum Chemistry. In *Proceedings of the 34th International Conference on Machine Learning (Proceedings of Machine Learning Research, Vol. 70)*, Doina Precup and Yee Whye Teh (Eds.). PMLR, 1263–1272.
- [11] Jiaqi Guan, Xingang Peng, Peiqi Jiang, Yunan Luo, Jian Peng, and Jianzhu Ma. 2023. LinkerNet: Fragment Poses and Linker Co-Design with 3D Equivariant Diffusion. In *Thirty-seventh Conference on Neural Information Processing Systems*.
- [12] Jiaqi Guan, Wesley Wei Qian, Xingang Peng, Yufeng Su, Jian Peng, and Jianzhu Ma. 2023. 3D Equivariant Diffusion for Target-Aware Molecule Generation and Affinity Prediction. In *International Conference on Learning Representations*.
- [13] Jonathan Ho, Ajay Jain, and Pieter Abbeel. 2020. Denoising Diffusion Probabilistic Models. In *Advances in Neural Information Processing Systems*, H. Larochelle, M. Ranzato, R. Hadsell, M.F. Balcan, and H. Lin (Eds.), Vol. 33. Curran Associates, Inc., 6840–6851.
- [14] L. Hu, M. L. Benson, R. D. Smith, M. G. Lerner, and H. A. Carlson. 2005. Binding MOAD (Mother Of All Databases). *Proteins* 60, 3 (2005), 333–340.
- [15] Laura Isigkeit, Tim Hörmann, Espen Schallmayer, Katharina Scholz, Felix F. Lillich, Johanna H. M. Ehrler, Benedikt Hufnagel, Jasmin Büchner, Julian A. Marschner, Jörg Pabel, Ewgenij Proschak, and Daniel Merk. 2024. Automated design of multi-target ligands by generative deep learning. *Nature Communications* 15, 1 (2024), 7946.
- [16] Wengong Jin, Dr.Regina Barzilay, and Tommi Jaakkola. 2020. Multi-Objective Molecule Generation using Interpretable Substructures. In *Proceedings of the 37th International Conference on Machine Learning (Proceedings of Machine Learning Research, Vol. 119)*, Hal Daumé III and Aarti Singh (Eds.). PMLR, 4849–4859.
- [17] Wengong Jin, Regina Barzilay, and Tommi Jaakkola. 2018. Junction Tree Variational Autoencoder for Molecular Graph Generation. In *Proceedings of the 35th International Conference on Machine Learning (Proceedings of Machine Learning Research, Vol. 80)*, 2323–2332.
- [18] Abbas Kabir and Aaron Muth. 2022. Polypharmacology: The science of multi-targeting molecules. *Pharmacological Research* 176 (2022), 106055.
- [19] Zhijia Li, Bo Yin, Shuangqian Zhang, Zhigang Lan, and Lan Zhang. 2023. Targeting protein kinases for the treatment of Alzheimer’s disease: Recent progress and future perspectives. *European Journal of Medicinal Chemistry* 261 (2023), 115817.
- [20] Haitao Lin, Guojiang Zhao, Odin Zhang, Yufei Huang, Lirong Wu, Cheng Tan, Zicheng Liu, Zhifeng Gao, and Stan Z. Li. 2025. CBGBench: Fill in the Blank of Protein-Molecule Complex Binding Graph. In *The Thirteenth International Conference on Learning Representations*.
- [21] Christopher A. Lipinski, Franco Lombardo, Beryl W. Dominy, and Paul J. Feeney. 1997. Experimental and computational approaches to estimate solubility and permeability in drug discovery and development settings. *Advanced Drug Delivery Reviews* 23, 1 (1997), 3–25.
- [22] Meng Liu, Youzhi Luo, Kanji Maruhashi, and Shuiwang Ji. 2022. Generating 3D Molecules for Target Protein Binding. In *International Conference on Machine Learning*.
- [23] Zhihai Liu, Yan Li, Li Han, Jie Li, Jie Liu, Zhixiong Zhao, Wei Nie, Yuchen Liu, and Renxiao Wang. 2014. PDB-wide collection of binding data: current status of the PDBbind database. *Bioinformatics* 31, 3 (2014), 405–412.
- [24] Fengqing Lu, Mufei Li, Xiaoping Min, Chunyan Li, and Xiangxiang Zeng. 2021. De novo generation of dual-target ligands using adversarial training and reinforcement learning. *Briefings in Bioinformatics* 22, 6 (2021), bbab333.
- [25] Shitong Luo, Jiaqi Guan, Jianzhu Ma, and Jian Peng. 2021. A 3D Generative Model for Structure-Based Drug Design. In *Thirty-Fifth Conference on Neural Information Processing Systems*.
- [26] Brenton P. Munson, Michael Chen, Audrey Bogosian, Jason F. Kreisberg, Katherine Licon, Ruben Abagyan, Brent M. Kuenzi, and Trey Ideker. 2024. De novo generation of multi-target compounds using deep generative chemistry. *Nature Communications* 15, 1 (2024), 3636.
- [27] Xingang Peng, Jiaqi Guan, Qiang Liu, and Jianzhu Ma. 2023. MolDiff: Addressing the Atom-Bond Inconsistency Problem in 3D Molecule Diffusion Generation. In *Proceedings of the 40th International Conference on Machine Learning (Proceedings of Machine Learning Research, Vol. 202)*, PMLR, 27611–27629.
- [28] Xingang Peng, Shitong Luo, Jiaqi Guan, Qi Xie, Jian Peng, and Jianzhu Ma. 2022. Pocket2Mol: Efficient Molecular Sampling Based on 3D Protein Pockets. In *International Conference on Machine Learning*.
- [29] Alexander S. Powers, Helen H. Yu, Patricia Suriana, Rohan V. Koodli, Tianyu Lu, Joseph M. Paggi, and Ron O. Dror. 2023. Geometric Deep Learning for Structure-Based Ligand Design. *ACS Cent. Sci.* 9, 12 (2023), 2257–2267.
- [30] Anjie Qiao, Yuting Chen, Junjie Xie, Weifeng Huang, Hao Zhang, Qirui Deng, Jiahua Rao, Ji Deng, Fanbo Meng, Zhen Wang, Mingyuan Xu, Hongming Chen, Jiancong Xie, Shuangjia Zheng, Yuedong Yang, Guo-Bo Li, and Jinping Lei. 2025. A 3D pocket-aware lead optimization model with knowledge guidance and its application for discovery of new glutamyl cyclase inhibitors. *Briefings in Bioinformatics* 26, 4 (07 2025), bbaf345.
- [31] Anjie Qiao, Hao Zhang, Qianmu Yuan, Qirui Deng, Jingtian Su, Weifeng Huang, Huihao Zhou, Guo-Bo Li, Zhen Wang, and Jinping Lei. 2025. A 3D pocket-aware and evolutionary conserved interaction guided diffusion model for molecular optimization. *arXiv preprint arXiv:2505.05874* (2025).
- [32] Matthew Ragoza, Tomohide Masuda, and David Ryan Koes. 2022. Generating 3D molecules conditional on receptor binding sites with deep generative models. *Chem Sci* 13 (7 Feb 2022), 2701–2713.
- [33] Victor Garcia Satorras, Emiel Hoogeboom, and Max Welling. 2021. E(n) Equivariant Graph Neural Networks. In *Proceedings of the 38th International Conference on Machine Learning (Proceedings of Machine Learning Research, Vol. 139)*, Marina Meila and Tong Zhang (Eds.). PMLR, 9323–9332.
- [34] Arne Schneuing, Charles Harris, Yuanqi Du, Kieran Didi, Arian Jamasb, Ilia Igashov, Weitao Du, Carla Gomes, Tom L. Blundell, Pietro Lio, Max Welling, Michael Bronstein, and Bruno Correia. 2024. Structure-based drug design with equivariant diffusion models. *Nature Computational Science* 4, 12 (01 Dec 2024), 899–909.
- [35] Thibaud Southirathn, Bonil Koo, Yijinxu Lu, and Sun Kim. 2025. CombiMOTS: Combinatorial Multi-Objective Tree Search for Dual-Target Molecule Generation. In *Forty-second International Conference on Machine Learning*.
- [36] Dejuan Sun, Yuqian Zhao, Shouyue Zhang, Lan Zhang, Bo Liu, and Liang Ouyang. 2020. Dual-target kinase drug design: Current strategies and future directions in cancer therapy. *European Journal of Medicinal Chemistry* 188 (2020), 112025.
- [37] Renxiao Wang, Xueliang Fang, Yipin Lu, and Shaomeng Wang. 2004. The PDBbind Database: Collection of Binding Affinities for Protein-Ligand Complexes with Known Three-Dimensional Structures. *J. Med. Chem.* 47, 12 (2004), 2977–2980.
- [38] Renxiao Wang, Xueliang Fang, Yipin Lu, Chao-Yie Yang, and Shaomeng Wang. 2005. The PDBbind Database: Methodologies and Updates. *J. Med. Chem.* 48, 12 (2005), 4111–4119.
- [39] Yaodong Yang, Guangyong Chen, Jinpeng Li, Junyou Li, Odin Zhang, Xujun Zhang, Lanqing Li, Jianye Hao, Ercheng Wang, and Pheng-Ann Heng. 2024. Enabling target-aware molecule generation to follow multi objectives with Pareto MCTS. *Communications Biology* 7, 1 (2024), 1074.
- [40] Jing Ye, Junhao Wu, and Bo Liu. 2023. Therapeutic strategies of dual-target small molecules to overcome drug resistance in cancer therapy. *Biochimica et Biophysica Acta (BBA) - Reviews on Cancer* 1878, 3 (2023), 188866.
- [41] Xiangxin Zhou, Jiaqi Guan, Yijia Zhang, Xingang Peng, Liang Wang, and Jianzhu Ma. 2024. Reprogramming Pretrained Target-Specific Diffusion Models for Dual-Target Drug Design. In *The Thirty-eighth Annual Conference on Neural Information Processing Systems*.
- [42] Hui Zhu, Xuelian Li, Baoquan Chen, and Niu Huang. 2025. Augmented BindingNet dataset for enhanced ligand binding pose predictions using deep learning. *npj Drug Discovery* 2, 1 (2025), 1.

A Dataset (BN2-DT) Derivation Details

Source and goal. BN2-DT is derived from the high-quality subset of BindingNet v2, where each record provides a single-target complex in the form (G, X, P) . Our goal is to derive dual-target tuples (G, X_1, X_2, P_1, P_2) for learning $p(G, X_1, X_2 | P_1, P_2)$, by pairing two single-target complexes that share the same ligand molecular graph while corresponding to two distinct pockets/targets. We use the high confidence subset to reduce noise from modeled poses, as BindingNet v2 provides confidence-ranked modeled complexes.

Pocket distinctness. We use $P_1 \neq P_2$ to indicate that the two complexes correspond to distinct binding contexts in BindingNet v2, rather than strict geometric non-overlap. Since pocket representations may differ in size/extent and are expressed in arbitrary coordinate frames across complexes, we treat $P_1 \neq P_2$ as meaning that the two pockets are not near-identical up to SE(3) rigid motions at the global level; in particular, partial local similarity or small perturbations may exist even when $P_1 \neq P_2$. In practice, we enforce distinctness primarily by target/pocket identifiers and use the geometric criterion only to avoid near-duplicate records when applicable.

Derivation protocol. We traverse BindingNet v2 (high confidence subset) and group single-target complexes by ligands with an identical molecular graph. To reduce redundancy, if the same ligand appears multiple times under the same target/pocket, we keep only one representative occurrence for that target. For each ligand that appears in at least two distinct targets/pockets, we then enumerate all *unordered* pairs of its occurrences across different targets and treat each pair as a candidate dual-target instance, inheriting the bound conformations from the two complexes as (X_1, X_2) . To ensure that the paired occurrences indeed share the same ligand graph (identical atom types and bond orders), we additionally perform a graph-isomorphism check between the two ligands and discard any mismatched pairs. Finally, we deduplicate candidate instances by treating $(\text{occ}_a, \text{occ}_b)$ and $(\text{occ}_b, \text{occ}_a)$ as the same pair and removing repeats.

Pocket extraction. For each complex, the pocket P is derived by selecting all standard amino-acid residues that contain at least one atom within 10 Å of any ligand atom (based on the ligand coordinates in the complex). The resulting residue set is used as the pocket representation in BN2-DT.

Statistics. From the BindingNet v2 high confidence subset, we obtain 197,488 ligands in total. Among them, 21,721 ligands appear in at least two targets/pockets and yield 58,058 dual-target training tuples in BN2-DT.

B Theoretical analysis

Proof of Proposition 3.2. We verify **R1–R4** in Def. 3.1.

R1 (Permutation invariance). Let π denote the operator that swaps the two targets: $\pi(P_1, P_2) = (P_2, P_1)$ and $\pi(G, X_1, X_2) = (G, X_2, X_1)$. We need to show $p_\theta(M^{(0)} | P) = p_\theta(\pi(M^{(0)}) | \pi(P))$.

First, the base distribution is symmetric: $p_{\text{base}}(X_1^{(T)}) = p_{\text{base}}(X_2^{(T)})$ and it does not privilege either target, hence $p_{\text{base}}(M^{(T)} | P) = p_{\text{base}}(\pi(M^{(T)}) | \pi(P))$.

Second, it suffices to show the denoiser $f_\theta(M^{(t)}, t, P)$ is permutation-equivariant w.r.t. swapping target indices. In each MPNN layer, FuseDiff constructs two point-cloud graphs $G_k^{(\ell)}$ and fuses them into an augmented graph $G_{\text{aug}}^{(\ell)}$. Swapping (P_1, P_2) exchanges the two point-cloud graphs but leaves the ligand subgraph unchanged. For ligand–ligand edges, the geometric features are built from the symmetric statistics $s_{uv}^{(\ell)} = d_{1,uv}^{(\ell)} + d_{2,uv}^{(\ell)}$ and $\delta_{uv}^{(\ell)} = |d_{1,uv}^{(\ell)} - d_{2,uv}^{(\ell)}|$, which are invariant under swapping the two targets. All node/edge updates are computed by shared MLPs and permutation-invariant aggregations (sums over neighbors), therefore swapping the targets permutes the resulting representations in the same way. Finally, the coordinate updates are carried out separately on each $G_k^{(\ell)}$; after swapping targets, the update for $k = 1$ becomes the update for $k = 2$ and vice versa. Hence $f_\theta(\pi(M^{(t)}), t, \pi(P)) = \pi(f_\theta(M^{(t)}, t, P))$, which establishes **R1**.

R2 (SE(3) invariance). We consider independent rigid motions $g, g' \in \text{SE}(3)$ applied to the two complexes, i.e., $(P_1, X_1) \mapsto (T_g P_1, T_g X_1)$ and $(P_2, X_2) \mapsto (T_{g'} P_2, T_{g'} X_2)$.

(i) The base distributions for $X_1^{(T)}$ and $X_2^{(T)}$ are isotropic Gaussians (restricted to the CoM-free subspace under the standard centering preprocessing used in SBDD diffusion), hence invariant under rotations and compatible with translation-free (CoM-free) coordinates.

(ii) In message passing, all geometric inputs injected into $G_{\text{aug}}^{(\ell)}$ are scalar distances (either $d_{k,uv}^{(\ell)}$ for pocket-involved edges or $(s_{uv}^{(\ell)}, \delta_{uv}^{(\ell)})$ for ligand–ligand edges), which are invariant under SE(3) transforms applied to the corresponding complex. Therefore the updated node/edge embeddings are invariant to rigid motions of either complex.

(iii) The coordinate update in each point-cloud graph $G_k^{(\ell)}$ is of the form (Eq. (7)) $\Delta r_{k,u}^{(\ell)} = \sum_{w \in N_k(u)} \psi(\cdot) \frac{r_{k,u}^{(\ell)} - r_{k,w}^{(\ell)}}{\|r_{k,u}^{(\ell)} - r_{k,w}^{(\ell)}\|_2}$, i.e., a scalar function of invariant inputs multiplying a relative displacement vector. Thus, for each k , the update is $O(3)$ -equivariant for X_k under rigid motions of the k -th complex. Moreover, since the k -th coordinate update uses only geometry from (P_k, X_k) , it is invariant to independent rigid motions applied to the other complex. This establishes **R2**.

R3 (Non-factorization). Although each reverse transition factorizes as $p_\theta(M^{(t-1)} | M^{(t)}, P) = \prod_{k=1}^2 p_\theta(X_k^{(t-1)} | M^{(t)}, P) \cdot p_\theta(G^{(t-1)} | M^{(t)}, P)$, the model density is obtained by marginalizing the latent trajectory:

$$p_\theta(M^{(0)} | P) = \int p_{\text{base}}(M^{(T)} | P) \prod_{t=1}^T p_\theta(M^{(t-1)} | M^{(t)}, P) dM^{(1:T)}.$$

Crucially, both $X_1^{(t-1)}$ and $X_2^{(t-1)}$ are conditioned on the shared latent state $M^{(t)} = (G^{(t)}, X_1^{(t)}, X_2^{(t)})$ which is integrated out. In graphical-model terms, $X_1^{(t-1)} \leftarrow M^{(t)} \rightarrow X_2^{(t-1)}$ makes them d-connected after marginalizing $M^{(t)}$, so the resulting joint need not factorize as $p(X_1, X_2 | G, P_1, P_2) = p(X_1 | G, P_1, P_2) p(X_2 | G, P_1, P_2)$. Therefore $X_1 \not\perp X_2 | (P_1, P_2, G)$, establishing **R3**.

R4 (Non-restricted support). FuseDiff never imposes a global rigid alignment constraint between the two target-specific complexes.

While DLCF couples the two targets through shared ligand embeddings computed on the fused augmented graph, the coordinate updates are performed *separately* within each point-cloud graph $G_k^{(\ell)}$. The displacement field for target k depends on target-specific geometric inputs such as the neighbor set $N_k(u)$ and distances induced by P_k . Since $P_1 \neq P_2$ in general, these inputs can vary independently across targets, allowing the sampled (X_1, X_2) to vary beyond a single shared rigid transform. Hence the support is not restricted to $\{(X_1, X_2) : \exists g \in SE(3) \text{ s.t. } X_1 = T_g X_2\}$, establishing R4. \square

C Single-target Pretraining Checkpoint for Fair Benchmarking

To control for differences in single-target pretraining data when benchmarking TARGETDIFF, DUALDIFF, and COMPDIFF on DDF, we compare two pretrained TARGETDIFF checkpoints: the official one pretrained on CrossDocked2020 (denoted as -CD) and our checkpoint pretrained on BindingNet v2 (denoted as -BN2). All methods are evaluated on the DDF benchmark with the same sampling and evaluation protocol. As shown in Tables 4–5, the two checkpoints lead to overall comparable performance across both chemical-property metrics and docking-based affinity metrics, indicating that the downstream comparisons are not driven by the particular choice of single-target pretraining data. We therefore use the -BN2 checkpoint as a common pretrained backbone in our main experiments for a controlled comparison.

Table 4: Checkpoint comparison on DDF (molecular properties). We report molecule-level metrics for TARGETDIFF, COMPDIFF, and DUALDIFF when using the official CrossDocked2020 pretrained checkpoint (-CD) versus our BindingNet v2 pretrained checkpoint (-BN2).

| Methods | Metrics | | | | |
|----------------|-------------------|------------------|-------------------|------|--------------------|
| | QED(\uparrow) | SA(\uparrow) | Div. (\uparrow) | logP | LPSK(\uparrow) |
| Ref. | 0.51 | 0.77 | 0.74 | 2.89 | 4.50 |
| TARGETDIFF-CD | 0.53 | 0.54 | 0.70 | 2.48 | 4.63 |
| TARGETDIFF-BN2 | 0.54 | 0.55 | 0.67 | 2.32 | 4.69 |
| COMPDIFF-CD | 0.57 | 0.58 | 0.72 | 3.67 | 4.54 |
| COMPDIFF-BN2 | 0.59 | 0.57 | 0.69 | 3.48 | 4.74 |
| DUALDIFF-CD | 0.59 | 0.61 | 0.67 | 3.43 | 4.67 |
| DUALDIFF-BN2 | 0.59 | 0.58 | 0.69 | 3.54 | 4.88 |

D Ablation Details

(1) *W/o bond generative modeling.* We ablate explicit bond-type generation by diffusing and sampling only atom types and coordinates, while still performing message passing and representation updates with DLCF on the augmented graph. Instead of predicting bond types from augmented edge representations via a dedicated bond head as in FUSEDIFF, we infer chemical bonds *post hoc* and *independently* for each pose from the shared atom types and the denoised coordinates. This decoupled reconstruction frequently yields pose-specific bond assignments that are mutually incompatible across X_1 and X_2 , preventing the recovery of a single molecular

graph consistent with both targets. As a result, **Dual-Validity** drops from 61% in the full model to 3% on DDF, indicating that generative bond modeling is essential for enforcing cross-pose topological consistency.

(2) *W/o DLCF.* We ablate Dual-target Local Context Fusion (DLCF) and thus do not fuse the two point-cloud graphs (Sec. 3.4.1) into a single augmented graph. To preserve topology consistency, a natural fallback is to sample sequentially under the two pockets while enforcing a shared ligand graph, resembling a straightforward extension of single-target SBDD. However, this strategy effectively marginalizes over the second pocket during the first-stage generation, making cross-target incompatibility systematic rather than incidental. Empirically, the resulting samples exhibit pronounced atom–bond inconsistencies (e.g., unphysical covalent distances and distorted conformations), deviating from realistic molecular geometries. Consequently, **Dual-Validity** drops to 2%, demonstrating that DLCF is necessary to realize joint conditionality (R3) without sacrificing geometric plausibility.

E Reference dual-target ligands of GSK3 β and JNK3

We curate ChEMBL actives for each pocket (GSK3 β : 2128; JNK3: 791) and identify ligands shared by both sets up to *2D graph isomorphism* (i.e., identical molecular graphs with potentially different atom indexing). This yields three shared ligands, which serve as reference dual-target ligands for qualitative comparison. For each reference ligand, we visualize its 2D structure and the binding poses in the GSK3 β and JNK3 pockets (Fig. 6).

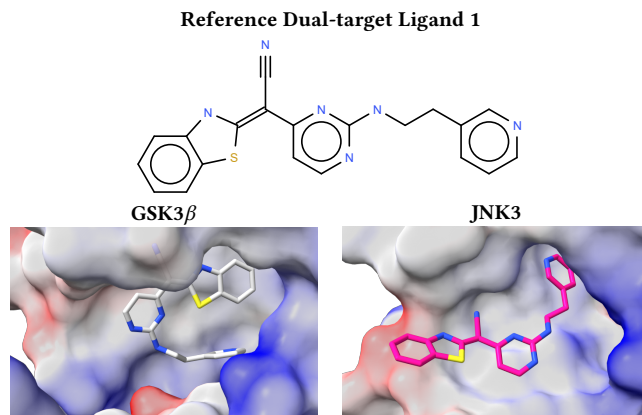


Table 5: Checkpoint comparison on DDF (docking-based affinity). Docking metrics on the two pockets (P1/P2) and their aggregate (Max Vina Dock), together with Dual High Affinity, for baselines using -CD versus -BN2 pretrained TARGETDIFF checkpoints.

| Methods | Metrics | | | | | | | | | |
|----------------|------------------|-------|-------|------------------|-------|-------|-------------------|-------|--------------------|-------|
| | P1-Vina Dock (↓) | | | P2-Vina Dock (↓) | | | Max Vina Dock (↓) | | Dual High Aff. (↑) | |
| | Avg. | Med. | LBE | Avg. | Med. | LBE | Avg. | Med. | Avg. | Med. |
| Ref. | -8.23 | -7.98 | -0.38 | -8.14 | -8.23 | -0.37 | -6.15 | -6.73 | - | - |
| TARGETDIFF-CD | -8.89 | -8.91 | -0.37 | -7.23 | -7.68 | -0.28 | -6.84 | -6.91 | 30.8% | 23.3% |
| TARGETDIFF-BN2 | -8.95 | -8.86 | -0.35 | -7.14 | -7.99 | -0.28 | -6.88 | -7.36 | 31.1% | 23.4% |
| COMPDIFF-CD | -8.35 | -8.46 | -0.36 | -8.35 | -8.37 | -0.36 | -7.53 | -7.84 | 37.9% | 31.4% |
| COMPDIFF-BN2 | -8.75 | -8.79 | -0.36 | -8.73 | -8.65 | -0.36 | -7.92 | -7.98 | 39.8% | 33.0% |
| DUALDIFF-CD | -8.46 | -8.52 | -0.38 | -8.45 | -8.52 | -0.38 | -7.77 | -7.79 | 39.3% | 31.9% |
| DUALDIFF-BN2 | -8.80 | -8.82 | -0.37 | -8.72 | -8.78 | -0.37 | -7.99 | -8.09 | 40.5% | 33.4% |

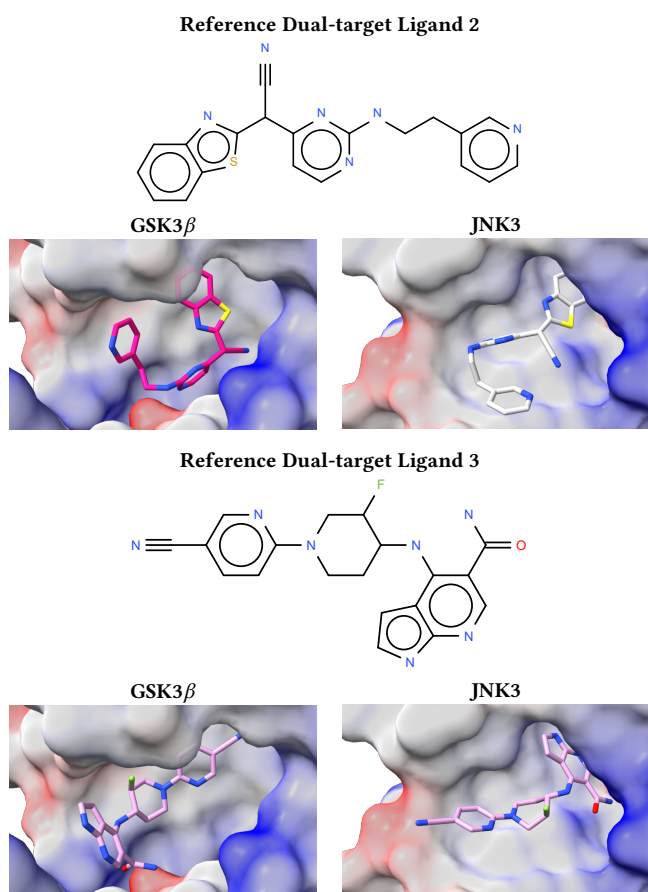


Figure 6: Reference dual-target ligands for GSK3 β and JNK3. Each ligand is shown with its 2D structure (top) and binding poses identified by an AutoDock Vina search in the GSK3 β (left) and JNK3 (right) pockets (bottom).